Mantle heterogeneity in the source region of mid-ocean ridge basalts along the northern Central Indian Ridge (8°–17°S)

Jonguk Kim[1*], Sang-Joon Pak[1], and Jai-Woon Moon[1], Deep-sea & Seabed Mineral Resources Research Center, Korea Institute of Ocean Science & Technology, 787, Haeanro, Ansan, 15627 Korea

Sang-Mook Lee[2], School of Earth and Environmental Sciences, Seoul National University, 1 Gwanakro, Gwanakgu, Seoul, 08826, Korea

.

Jihye Oh[1], Deep-sea & Seabed Mineral Resources Research Center, Korea Institute of Ocean Science & Technology, 787, Haeanro, Ansan, 15627 Korea

Finlay M. Stuart[3], Isotope Geoscience Unit, Scottish Universities Environmental Research Center, East Kilbride G75 0QF, UK

*Corresponding author: Jonguk Kim, Deep-sea & Seabed Mineral Resources Research Center, Korea Institute of Ocean Science & Technology, 787, Haeanro, Ansan, 426-744 Korea (jukim@kiost.ac.kr)

Key Points

- Examination of origin of E-MORB far from hotspots in the Central Indian Ridge
- E-MORB in southern segment affected by fossil Rèunion mantle component
- E-MORB independent from hotspot in northern segment show FOZO composition

Abstract

The northern Central Indian Ridge (CIR) between 8°S and 17°S is composed of seven segments whose spreading rates increase southward from ~35 to ~40 mm/yr. During expeditions of R/V *Onnuri* to study hydrothermal activity on the northern CIR in 2009 to 2011, high-resolution multibeam mapping was conducted and ridge axis basalts were dredged. The major and trace element, and Sr–Nd–Pb-He isotopic compositions of basaltic glasses dredged from the spreading axis require three mantle sources; depleted mantle and two distinct enriched mantle sources. The southern segments have Sr, Nd, and Pb that are a mix of depleted mantle and an enriched component as recorded in southern CIR MORB. This enrichment is indistinguishable from Rèunion plume mantle, except for He isotopes. This suggests that the southern segments have incorporated a contribution of the fossil Rèunion plume mantle, as the CIR migrated over hotspot-modified mantle. The low $^{3}He/^{4}He$ (7.5 to 9.2 R_A) of this enriched component may result from radiogenic ^{4}He ingrowth in the fossil Rèunion mantle component. Basalts from the northern segments have high $^{206}Pb/^{204}Pb$ (18.53-19.15) and low $^{87}Sr/^{86}Sr$ (0.70286-0.70296) that are distinct from the Rèunion plume but consistent with derivation from mantle with FOZO signature, albeit with $^{3}He/^{4}He$ (9.2 to 11.8 R_A) that are higher than typical. The FOZO-like enriched mantle cannot be attributed to the track of a nearby mantle plume. Instead, this enrichment may have resulted from recycling oceanic crust, possibly accompanied by small plume activity.

Index terms: 1032 Geochemsitry: Mid-Oceanic ridge processes (3614, 8416); 1038 Geochemistry: Mantle processes (3621); 1065 Geochemistry: Major and trace element geochemistry; 1040 Geochemistry: Radiogenic isotope geochemistry

Keywords: MORB; Central Indian Ridge, mantle heterogeneity, Rèunion hotspot, FOZO

1. Introduction

The depleted upper mantle has been considered as the main source of mid-ocean ridge basalts (MORB) [*Hart*, 1971]. In addition, upwelling mantle plumes are an important source of geochemical heterogeneity in the upper mantle. The presence of geochemically and isotopically enriched mid-ocean ridge basalts (E-MORBs) has been explained by the melting of plume mantle and depleted upper mantle [*Schilling*, 1985, 1973]. It is generally thought that the extent to which actively upwelling hotspot mantle is incorporated into ridge melt regime depends on the distance between the two features. The enriched mantle components and E-MORB found on ridges close to hot spots can be explained by mixing with mantle plume components, but the origin of E-MORB far from hotspots is more controversial [i.e. *Donnelly et al.*, 2004; *Ulrich et al.*, 2012; *Waters et al.*, 2011]. The occurrence of E-MORB in ridge segments located far from any plumes suggests that enriched sources irrelevant to hotspot plumes, for example, recycling of metasomatized mantle or OIB/seamount material through subduction, are ubiquitous in the upper mantle [*Donnelly et al.*, 2004; *Ulrich et al.*, 2012]. Waters et al. (2011) proposed that E-MORB in the9°–10°N region of the EPR is produced through the same plumbing system as N-MORB, by mixing of deeply generated garnet pyroxenite melts with shallowly generated accumulated proxenite-peridotite melt. The occurrence of E-MORB uninfluenced by plumes likely indicates smaller heterogeneities dispersed in the mantle.

This study examines the relationship between mid-ocean ridges and hotspots in the area of the Central Indian Ridge (CIR) located more than 1000 km from the Rèunion hotspot. The CIR provides an ideal opportunity to explore distant ridge–hotspot interactions. Along

the CIR, the Marie Celeste Fracture Zone (MCFZ, Fig. 1) represents a major offset marking the boundary between the northern and southern CIR. The influence of the Rèunion hotspot on the CIR has been previously demonstrated by systematic sampling and analysis of MORB glasses from the southern CIR [*Furi et al.*, 2011; *Murton et al.*, 2005; *Nauret et al.*, 2006]. *Mahoney et al.* [1989] documented Rèunion-like radiogenic isotope signatures in basalt glasses from near the MCFZ, yet to date there has been no systematic petrological or geochemical investigations of the CIR north of the MCFZ.

Here, we present the first systematic geochemical and isotopic analyses of MORB glasses collected from seven segments of the CIR north of the MCFZ, between 8°S and 17°S. We show the presence of at least three distinct mantle sources in the northern CIR: (1) depleted mantle; (2) an enriched mantle component mainly observed in the southern segments; and (3) a second enriched mantle component in the northern segments. The distinct E-MORB compositions enable us to examine the origins of these mantle heterogeneities.

2. Geological setting

The Central Indian Ridge is a slow–intermediate (~34 to 40 mm/yr *DeMets et al.*, [2010]) spreading ridge with morphology typical of slow spreading ridges; it has a 500–1000-m-deep axial valley and 50–100 km long segments connected by short transform faults and non-transform discontinuities [*Parson et al.*, 1993]. The ridge extends northward from the Rodrigues Triple Junction at ~25°S to the Owen Fracture Zone at ~10°N. The study area is located between 8°S (near the Chagos Laccadive Ridge) and 17°S (north of the MCFZ). Although bathymetric data are available in the northern and southern parts of the study area [*Drolia et al.*, 2005; *Dyment et al.*, 1999], prior to our survey no high-resolution swath multibeam bathymetric surveys had been undertaken.

The ridge studied here is composed of seven spreading segments (90-110 km long). Each segment is terminated by transform faults (Fig. 1), each with a similar length of ~90-110 km, apart from segments 1 and 2 that are separated by a long fault (~240 km) known as the Vema Fracture Zone. The structure of the transform fault between segments 3 and 4 is poorly defined. Both the bathymetric and backscatter multibeam echo data indicate that an active rift valley only exists in the southern half of segment 4, between 11°20′S and 11°40′S. The neovolcanic zone of the spreading segments is evident from the development of a rift valley with high backscatter. Spreading segment 4 (a short segment) is connected to segment 3 by an oblique trough, as indicated by a high-backscatter region in the acoustic imagery that extends from the southern end of segment 3 (see the Supplementary Material, Appendix Figure S1).

The Rèunion hotspot is currently ~1100 km to the west of the ridge axis (Fig. 1). The Rèunion hotspot formed the Deccan Traps around the time of the KT boundary (~65-66 Ma), and then the plume formed the Laccadives-Maldives-Chagos ridges, and much of the Mascarene Plateau, including the young volcanic island of Mauritius [*Duncan*, 1990]. The CIR transected the Rèunion-Mauritius hotspot track at ~34 Ma. Plate reconstruction suggests that the Chagos was originally joined to the Mascarene Plateau [*Torsvik et al.*, 2013]. Thus, the trajectory of past Rèunion hotspot activity from the southern end of the Chagos–Laccadives Ridge can be extended to the CIR section of our study. The east–west trending Rodrigues Ridge and smaller en-echelon volcanic ridges at 19°S (the Three Magi Ridges and the Gasitao Ridge) appear to connect the Rèunion–Mauritius hotspot track to the present-day CIR axis. *Mahoney et al.* [1989] and *Murton et al.* [2005] proposed that E-MORB were produced by eastward migration of Rèunion hotspot mantle along the MCFZ toward the CIR. However, more detailed sampling along axis of the CIR segment located south of the MCFZ suggested that direct mantle flow from the Rèunion hotspot would meet the CIR not at ~18°S,

immediately south of the MCFZ but at ~19.5°S, near the present-day intersection of the CIR and the off-axis ridges [*Furi et al.*, 2011; *Nauret et al.* 2006]. Thus, the mantle-source enrichment observed near the MCFZ is unrelated to direct mantle flow from the Rèunion hotspot.

3. Sampling and analytical methods

The samples analyzed in this study were obtained during three annual cruises of the R/V *Onnuri*, as part of the Korea Deep Ocean Study (KODOS) program that investigated the CIR during 2009–2011. Fresh basalt samples with glassy chilled margins were dredged from 53 stations along 7 spreading axes at an average interval of ~20 km. Samples were crushed, sonicated in distilled water until no turbidity was observed, and then dried. Glass fragments were hand-picked under a binocular microscope to exclude alteration. Prior to final grinding, the samples were leached in 1 M HCl for 10 minutes at room temperature to remove carbonate.

Major and trace element compositions were determined on 75 samples. Samples were prepared and analyzed in batches. Each batch contained a reagent blank, a certified reference material, and 17% duplicate samples. Samples were mixed with a flux of $LiBO_2$ and $Li_2B_4O_7$ and fused in an induction furnace. The melt was immediately poured into a solution of 5% HNO_3 containing an internal standard, and mixed continuously until completely dissolved (~30 minutes). The samples were analyzed for major oxides and selected trace elements using a combination of simultaneous/sequential ICP–AES (Thermo Jarrell-Ash ENVIRO II) and ICP–MS (Perkin-Elmer ELAN 6000) by Activation Laboratories, Canada. Calibration was performed using seven USGS and CANMET certified reference materials. One of the seven standards was analyzed as an unknown during the analysis of every group of 10 samples. The

uncertainty in the external reproducibility of the analyses was generally within ±5% except for some trace elements of which concentration is near the detection limit (Appendix Table S1).

Sr, Nd, Pb isotopes were determined in thirty samples He isotope composition determined in 38 samples. Sr and Nd isotopes were determined by thermal ionization mass spectrometry (TIMS, a ThermoFisher TRITON Plus) at the National Oceanographic Center (NOC). Samples for Sr and Nd were digested with HF/HNO_3, and the samples were collected in an HCl mother solution that was sub-sampled to give 1 μg of Sr and Nd. The Sr solution was processed using ~50-μl columns containing Sr-Spec resin and eluted with 3 M HNO_3 to remove interfering elements, followed by collection of the Sr in water. The purified Sr sample was dried and loaded onto a single Ta filament using a Ta activator solution, and the isotopic composition determined using a multi-dynamic peak jumping routine in a Thermo Fisher Triton Plus thermal ionization mass spectrometer. Beam intensities were maintained at 2V. Analyses of the NBS987 standard (n = 23) yielded an average $^{87}Sr/^{86}Sr$ of 0.710243 ± 0.000018 (2σ).

Solutions for Nd were first passed through a cation column to remove major cations and Ba using 2.2 M HCl, followed by collection of the rare earth elements (REE) in 6 M HNO_3. The Nd was then separated using an Ln-Spec column with 0.15 M HCl. The solution was dried and loaded onto the Ta side of a Ta–Re–Ta triple filament. The Nd isotopes were determined using a Thermo Fisher Triton Plus thermal ionization mass spectrometer using a multi-dynamic peak jumping routine and JNdi as a standard. Measured values for the JNdi standard were $^{143}Nd/^{144}Nd$ = 0.512092 ± 15 (2σ, n = 23), which is slightly lower but comparable with the value ($^{143}Nd/^{144}Nd$ = 0.512115 ± 7) of JNdi reported by *Tanaka et al.* [2000].

For the Pb isotope analysis, glass samples were dissolved in $HF/HNO_3/HBr$ and the Pb was purified using a two-stage anion column with HBr medium. The amount of Pb in procedural blanks was <50 pg, which is negligible relative to the amount of Pb recovered. The samples were analyzed in static mode on a Thermo Fisher Neptune MC–ICP–MC at the National Oceanographic Center (NOC), using a double spike technique to correct for fractionation and mass bias. Detailed description of Pb isotope analyses is given in *Taylor et al.* [2015]. The 2σ uncertainties on standard NBS 981 ($^{206}Pb/^{204}Pb$ = 16.9412; $^{207}Pb/^{204}Pb$ = 15.4988; $^{208}Pb/^{204}Pb$ = 36.7233) were 0.0025, 0.0025, and 0.0075 for $^{206}Pb/^{204}Pb$, $^{207}Pb/^{204}Pb$, and $^{208}Pb/^{204}Pb$, respectively.

Helium isotopes were measured in 1-3 mm fragments of alteration-free basalt glass that had been previously cleaned in analar acetone. Gases were extracted by in vacuo crushing 1-2 g of glass in a multi-sample hydraulic crusher. The extracted gases were purified by exposure to two hot GP50 ZrAl alloy getters and the heavy noble gases (Ar, Kr, Xe) were absorbed onto liquid nitrogen-cooled charcoal prior to analysis. The isotopic composition of the helium was measured by a MAP 215-50 mass spectrometer in static mode at SUERC [*Stuart et al.,* 2000; *Williams et al.,* 2005]. Blanks levels were measured each day and never exceeded 0.1% of the measured He. Mass spectrometer sensitivity and mass fractionation was determined by repeated analysis of aliquots from a reservoir of the HESJ international standard (20.63 R_A, *Matsuda et al.,* [2002]). The reproducibility of He isotope ratios is typically ±0.5% (1σ). The He concentrations reported in Table 1 are minimum estimates of the inventory of vesicle-hosted He as the in vacuo crushing process does not pulverise samples to powder.

4. Results

196 4.1. Major and trace elements

197 Major and trace element compositions are presented in Appendix Table S1. Most are
198 low-K tholeiitic basalts and show slight loss on ignition, indicating that alteration has been
199 minor. Major element concentrations show a generally negative correlation with MgO over
200 the range 6.9 to 9.2 wt.% (Appendix Fig. S3). Al_2O_3 and CaO display positive correlations
201 with MgO. These variations are typical of MORBs and reflect early fractional crystallization
202 of olivine and plagioclase with minor contribution of clinopyroxene.

203 Basalts have a wide variation in incompatible element and light rare earth element
204 (LREE) concentrations, ranging from N-MORB to E-MORB patterns (Fig. 2). There is little
205 systematic latitudinal variation in trace element patterns (Fig. 2). For example the most
206 depleted basalts occur in segment 1 in the north and segment 6 in the south. Although basalts
207 from the southern-most segment 7 show the most enriched compositions, basalts from other
208 segments tend to show transitional compositions. The basalts have trace element
209 compositions that lie between the depleted CIR MORB (sample RC14 of *Murton et al.*,
210 [2005]) and Rèunion basalts [*Albarede et al.*, 1997].

211 Trace element proxies for mantle fertility such as La/Sm and Nb/Zr do not differ
212 significantly in basalts from the northern and southern segments. Basalts from the northern
213 segments appear to have small range, and lower $(La/Sm)_N$ and Nb/Zr, than segments 5 to 7
214 (Fig. 3a). This likely reflects a less or different enriched source(s) for the northern segments
215 compared to the southern segments. Several basalts from the northern segments have higher
216 Ba/La for a given $(La/Sm)_N$. This suggests that a small contribution of an additional enriched
217 source, possibly related to the recycled oceanic crustal components, may be present in the
218 melting zone in the north.

219

220 4.2. Isotopic compositions

221 The isotopic composition of Sr, Nd, and Pb are presented in Table 1 and Fig. 4. Sr
222 ($^{87}Sr/^{86}Sr$ = 0.7028-0.7032) and Nd isotopes ($^{143}Nd/^{144}Nd$ = 0.51296-0.51322) display a
223 negative correlation that is typical of the global MORB data set (Fig. 4). With the exception
224 of three samples from southern segments that have more radiogenic Nd, all glasses plot in the
225 range of CIR MORB, significantly less radiogenic than Rèunion basalts [*Bosch et al.*, 2008;
226 *Nauret et al.*, 2006; *Escrig et al.*, 2004; *Mahoney et al.*, 1989]. In the $^{87}Sr/^{86}Sr$–$^{143}Nd/^{144}Nd$
227 space, the analyzed CIR basalts show a curvilinear trend, suggesting mixing between
228 depleted MORB with a seawater component and more enriched component (i.e. Rèunion
229 mantle). The elevated Sr isotopes of the three high $^{143}Nd/^{144}Nd$ samples might be indicative
230 of seawater alteration or isotopic heterogeneity in the Indian mantle source. The majority of
231 samples have less radiogenic Sr and more radiogenic Nd than MORB form the southern CIR
232 [*Nauret et al.*, 2006].

233 Pb isotopic compositions ($^{206}Pb/^{204}Pb$ = 17.91–19.15; $^{207}Pb/^{204}Pb$ = 15.46–15.62;
234 $^{208}Pb/^{204}Pb$ = 37.77–39.02) are more variable than Sr and Nd. Most samples show Pb isotope
235 ratios that overlap with those reported previously for CIR MORB [*Bosch et al.*, 2008; *Escrig*
236 *et al.*, 2004; *Mahoney et al.*, 1989; *Nauret et al.*, 2006]. The data define a distinct linear array
237 in both $^{207}Pb/^{204}Pb$–$^{206}Pb/^{204}Pb$ and $^{208}Pb/^{204}Pb$–$^{206}Pb/^{204}Pb$ space (Fig. 4). All analyzed
238 basalts plot above the Northern Hemisphere Reference Line (NHRL, Hart, [1984]), indicative
239 of the DUPAL signature which is typical of Indian MORB [*Dupre and Allegre*, 1983]. Three
240 basalts from segments 2 and 4 have compositions that are as, or more, radiogenic than
241 Rèunion basalts [*Nauret et al.*, 2006] (Fig. 4). The enrichment of Ba/La observed in some
242 basalts from the northern segments (Fig. 3) appears to be reflected in the Pb isotopic
243 compositions. Namely, the basalts showing high Ba/La from the northern segments also have

more radiogenic Pb isotope compositions (Fig. 5).

Helium isotope ratios vary between 7.5 and 11.8 R_A, where R_A is the atmospheric ratio (Table 1). This is similar to the range measured in glasses from the southern CIR [*Furi et al.*, 2011]. Four basalt samples in *Furi et al.*, [2011], recovered from segment 7 of our study, have similar $^3He/^4He$ as well as $(La/Sm)_N$ ratios to basalts from same segment (Fig. 6). The majority of the ridge is characterized by $^3He/^4He$ that is indistinguishable from the canonical values of depleted MORB-source mantle (8±1 R_A, *Graham*, [2002]). Basalts from the northern part of the ridge show two regions where $^3He/^4He$ are systematically higher than depleted MORB mantle values; segment 2 and segment 4 plus the south end of segment 3. The ^3He enrichment is likely associated with more primitive, less-degassed mantle source [e.g. *Stuart et al.*, 2003].

5. Discussion

5.1. Along-ridge geochemical variation

Although absolute concentrations of incompatible elements can be affected by fractional crystallization, effects on incompatible trace element ratios are insignificant [e.g., *Schilling and Winchester*, 1967; 1969; *Gast*, 1968] (Appendix Fig. S4). The concentration of Na_2O calculated at MgO = 8 wt.% (Na_8) shows limited variation, apart from at two dredge sites located in the oblique trough between segments 3 and 4, where high Na_8 values suggest a low degree of melting along a non-transform boundary. The Na_8 values do not correlate with ridge bathymetry (Fig. 5 and Appendix Fig. S4). This suggests that there is limited variation in the degree of partial melting along the ridges. In addition, no significant correlation is observed between $(La/Sm)_N$ and Na_8 in general, and from segment 4 in

267 particular (Fig. 5). This implies that the observed variations in incompatible trace elements
268 and isotope ratios are most likely related to source heterogeneity.

269 Trace element (e.g. $(La/Sm)_N$, Ba/La) and Sr–Nd–Pb-He isotopic composition of the
270 basalts show significant along-ridge variation (Fig. 5). Enriched basalts compositions are
271 more common in the southern segments (5-7). For instance, MORB from segments 6 and 7
272 show segment-scale variation (i.e. decrease of $(La/Sm)_N$ and Ba/La from north to south, Fig.
273 5d). Isotopic compositions of Sr, Nd, and Pb show even more distinct compositional
274 differences between segments. MORB from the segments 2 and 4 are characterized by more
275 radiogenic Sr and Pb and less radiogenic Nd isotope ratios than the segment immediately to
276 the south (segment 5) but not those segments farther away (segments 6 and 7). The isotopic
277 variation along the southern segments (5-7) is greater than in the northern segments and show
278 latitudinal variations in segment-scale similar to trace element ratios. For example,
279 $^{206}Pb/^{204}Pb$ ratios show a compositional trend that is similar to $(La/Sm)_N$ and Ba/La.

280 The trace element ratios and isotopic compositions indicate that the basalts along the
281 northern CIR are not derived from the homogeneous asthenosphere, but require contributions
282 from some heterogeneous and enriched mantle sources. For example, La/Sm varies by more
283 than one order of magnitude in global MORB (Hofmann, 2007). The pattern of compositional
284 variation of the basalts along the segments implies that the heterogeneity of CIR melting
285 regime can be attributed to local, small-scaled enriched sources, rather than a regional
286 heterogeneities such as from nearby mantle plume. The compositional variation of the basalts
287 from the northern segments appears to correlate with the helium isotope composition (Fig. 7).
288 MORB glasses with $^{3}He/^{4}He \leq 9.2\ R_A$ generally display negative correlations with $^{87}Sr/^{86}Sr$,
289 $^{206}Pb/^{204}Pb$, $(La/Sm)_N$, and Ba/La ratios, regardless of location. This trend of decreasing
290 $^{3}He/^{4}He$ with higher $^{87}Sr/^{86}Sr$ and La/Sm is commonly observed in MORB when $^{3}He/^{4}He$ is

below 10 R_A, particularly those in the Indian Ocean away from high $^3He/^4He$ hotspots. It can be attributed to melting of lithologic heterogeneities that may be globally dispersed in the asthenosphere [*Graham et al.*, 2014]. MORB glasses with $^3He/^4He \geq 9.2$ R_A from the northern segments plot on trends that are distinct from those defined by southern segment basalts. The high $^3He/^4He$ broadly correlates with $^{206}Pb/^{204}Pb$ and Ba/La but not $^{87}Sr/^{86}Sr$ and $(La/Sm)_N$.

The complex pattern of isotopes and trace element geochemistry requires the presence three mantle sources; depleted mantle and two distinct enriched mantle sources. This is most clearly seen in the Sr, Nd, and Pb isotopic data. For example, a plot of $^{87}Sr/^{86}Sr$ versus $^{206}Pb/^{204}Pb$ shows the two distinct enrichment trends. The trend to radiogenic Pb component is defined by MORB from the northern segments (Fig. 8A). The second trend, to radiogenic Sr mantle, is dominantly defined by MORB from the southern segments but includes a few MORB from the northern segments (Fig. 8A). The enrichment trend in the southern segments (including some samples from the northern segments) is similar to that of basalts from the southern CIR, and their composition tends towards that of samples from the Gasitao Ridge and Rèunion hotspot [*Nauret et al.*, 2006]. The enrichment exhibited by the northern segment MORB glasses is characterized by more radiogenic $^{206}Pb/^{204}Pb$ values for given $^{87}Sr/^{86}Sr$ (Fig. 8A). The enrichment trends in the northern and southern segments appear to correspond to the HIMU-like (or FOZO) and EM2 compositions respectively (Fig. 8C) [*Stracke et al.*, 2005]. Similar trends are evident in $^{143}Nd/^{144}Nd$-$^{208}Pb/^{206}Pb$ space (Fig. 8D).

5.2. Enriched mantle source in the southern segments: the Rèunion plume component

The Sr-Nd-Pb isotope compositions of MORB from southern segments plot along a mixing trend defined by basalts from the southern CIR, the Gasitao Ridge, and the Rèunion

315 hotspot (Fig. 8). Thus the compositional variation observed in the MORB in the southern
316 segments is more likely to originate from variation in the proportion of Rèunion component
317 mantle rather than other enrichment processes unrelated to hotspot plume. It should be noted
318 that the data demonstrate a significantly smaller proportion of this component than in the
319 basalts from the CIR sections further south (i.e. south of MCFZ, Fig. 6).

320 Previous studies have suggested that mantle flow from the Rèunion plume is blocked
321 by the MCFZ, and that the flow is diverted to the south along the CIR [*Mahoney et al.,* 1989;
322 *Murton et al.,* 2005; *Nauret et al.,* 2006]. *Nauret et al.* [2006] argued that basalts collected
323 near the MCFZ could have been derived from a second enriched mantle source, perhaps
324 produced by metasomatism. The enriched basalts from the southern ridge segments analyzed
325 here show geochemical affinities with MORB from south of the MCFZ. If this is the case,
326 then the discrepancy between *Nauret et al.* [2006] and this study, in terms of the origin of
327 enrichment observed in basalts from near the MCFZ, needs to be addressed.

328 The $^{3}He/^{4}He$ of the southern basalts (7.5 to 9.2 R_A) overlaps those of MORB from
329 immediately south of the MCFZ (7.1 to 10.9 R_A, Fig. 6). $^{3}He/^{4}He$ in both cases are
330 significantly lower than typical of Rèunion basalts (13-14 R_A; *Graham et al.,* [1990];
331 *Burnard et al.,* [1994]). *Furi et al.* [2011] argued that the low $^{3}He/^{4}He$ of the near- MCFZ
332 MORB can be explained by either: (1) radiogenic ^{4}He ingrowth in fossil Rèunion hotspot
333 mantle component, or (2) metasomatization of the depleted upper mantle. In either case, the
334 helium isotope composition of basaltic glasses can be explained by modification of the initial
335 He isotope composition by pre-eruptive ingrowth of radiogenic ^{4}He over time.

336 Contamination by fossil Rèunion hotspot component appears to be consistent with
337 paleogeographic reconstructions of the Indian plate, whereby the northern CIR transected the
338 Rèunion hotspot track [*Chatterjee et al.,* 2013]. The major tectonic and magmatic features of

339 the Indian Ocean show that the Deccan–Rèunion trail is disconnected by spreading at the CIR.
340 The trajectory of past Rèunion hotspot activity from the southern end of the Chagos–
341 Lacadives Ridge can be extended to CIR segments of our study (Fig. 1). Thus, the fossil
342 Rèunion mantle component could have been incorporated into the melting regime of those
343 spreading segments, if it is still present in the mantle beneath the CIR. The extent of mixing
344 of the fossil Rèunion component is limited to the scale of individual segments. For example,
345 the latitudinal variations in trace element and isotope ratios (Fig. 5) are different for each of
346 the segments in the southern CIR (especially in segment 6).

347 The influence of the Rèunion component on the CIR segments is also supported by
348 the mixing model shown in Fig. 9. On a $^{87}Sr/^{86}Sr$ versus $^{206}Pb/^{204}Pb$ plot, most of the MORB
349 from the CIR segments define a compositional array along a mixing curve between most-
350 depleted CIR MORB (RC14, *Murton et al.*, [2005]) and basalt of Rèunion trail with an age of
351 33 Ma (ODP115 site 706, *White et al.*, [1990]; *Greenough and Fryer*, [1990]) which
352 corresponds with the time of the CIR passed over the Rèunion hotspot (~34 Ma, *Duncan et*
353 *al.*, [1990]; *Torsvik et al.*, [2013]). A similar mixing trend can be observed in a $(La/Sm)_N$ vs.
354 $^{206}Pb/^{204}Pb$ space, although the data shows more scatter (Fig. 9B, D). Two end-member
355 compositions for the fossil Rèunion component are presented in Fig. 9. Rèunion trail basalts
356 have La/Sm ratios similar to most enriched MORB of this study [*Greenough and Fryer*,
357 1990]. However, more trace element enriched samples can be found in basalts from the
358 Rèunion Island [*Albarede et al.*, 1997]. Using the enriched Rèunion basalt only show slight
359 change of mixing curve in $^{87}Sr/^{86}Sr$ versus $^{206}Pb/^{204}Pb$ space (Fig. 9 A and C). Fig. 9 also
360 illustrates that some basalts from the northern segments plot along the Rèunion-depleted
361 mantle mixing curve. Thus, the fossil Rèunion plume mantle is not restricted to the southern
362 segments but extend to the northern segments. This is not surprising because the trajectory of
363 the past Rèunion hotspot pass through the middle of CIR segments of this study. Therefore,

364 the incorporation of the fossil Rèunion mantle component into the melting regime might be a
365 plausible enriched source responsible for major geochemical variation observed along the
366 entire CIR segments of this study.

367

368 5.3. Enriched mantle source in the northern segments: HIMU or FOZO component?

369 A second geochemically distinct enriched component is present in MORB from the
370 northern segments. The enrichment is characterized by radiogenic Pb isotopic signature (up
371 to 19.15 in $^{206}Pb/^{204}Pb$), high $^{3}He/^{4}He$ (up to 11.8 R_A) (Figs. 7 and 8) and enrichment of some
372 incompatible element ratios, such as Ba/La (Fig. 3). Although the enriched basalts from the
373 northern segments also have slightly more radiogenic Sr and less radiogenic Nd isotope ratios
374 than depleted MORB, the degree of enrichment is not significant as seen for Pb isotope ratios.
375 The Sr, Nd, and Pb isotope characteristics observed in the enriched MORB from the northern
376 segments appears to be explained by mixing of depleted mantle and HIMU-like mantle
377 [*Stracke et al.*, 2005] which is characterized by moderately more radiogenic in Sr, less
378 radiogenic in Nd, but significantly more radiogenic in Pb isotopes than depleted MORB (Fig.
379 8). The absence of active plume-related volcanism near our study area (other than Rèunion)
380 implies that the E-MORB from the northern segments can only be explained in terms of
381 MORB enrichment that is unrelated to hotspot activity.

382 Both "C" component (common component) [*Hanan and Graham*, 1996] and FOZO
383 (Focal Zone) [*Hart et al.*, 1992; *Hauri et al.*, 1994]) are proposed for representing common or
384 ubiquitous mantle components, based on the convergence of isotopic arrays of global MORB
385 ("C") and OIB (FOZO) data plots. "C" and FOZO have similar Pb isotope compositions but
386 the original definition of FOZO by *Hart et al.*, [1992] does not actually have the same Sr and
387 Nd isotope compositions as the "C" composition. *Stracke et al.*, [2005] redefined the isotopic

composition of original FOZO to overlap and extend the MORB array (i.e. “C” composition), which expand the FOZO concept as a common component in MORB and many OIB sources (Fig. 8). They also interpreted the origin of that component to be derived by subduction and aging of ocean crust recycled through the lower mantle as *Hanan and Gragam* [1996] inferred similarly for the origin of “C” component.

The recycling of oceanic crust for origin of FOZO generally corresponds to the genetic models for hotspot-unrelated E-MORB [*Donnelly et al.*, 2004; *Ulrich et al.*, 2012]. *Donnelly et al.* [2004] suggested that E-MORBs can be generated by the addition of enriched sources produced by subduction-related metasomatism during partial melting under a ridge. More recently, *Ulrich et al.* [2012] proposed that the recycling of ocean island basalts (OIBs)/seamounts is a plausible mechanism for producing the enriched sources that generate E-MORBs. Examples provided by *Donnelly et al.* [2004] and *Ulrich et al.* [2012] of local E-MORBs from the Mid-Atlantic Ridge at ~23°N and at ~15°20′N also show “FOZO-like” isotopic trends that are similar to those observed in our data (Fig. 8), thereby supporting a common process of MORB enrichment in areas located far from hotspots; i.e. a ubiquitous FOZO component in MORB sources. Recent seismic tomographic studies showed subducted slab materials descend into to lower mantle [e.g. Fukao and Obayashi, 2013; Fukao et al., 2001; Grand et al., 1997]. If subducted material is recycled through both the shallow mantle and through the deep source of mantle plumes, as proposed by *Li et al.* [2014], continuous subduction can cause compositionally heterogeneity with the FOZO-like component in lower mantle as well as upper mantle.

The isotopic variation observed in the northern segments of CIR is well explained by a mixing between depleted samples of CIR and the basalt sample from Young Rurutu [*Chauvel et al.*, 1997; *Vlastelic et al.*, 2009] representing FOZO component (Fig. 9). Fig. 9

412 also shows geochemical affinity of the enrichment in the northern segments with HIMU
413 component. Both FOZO and HIMU components are characterized by enrichment of
414 radiogenic Pb isotopes, reflecting their genetic process related to recycling of oceanic crust.
415 Contrary to the redefined FOZO component, however, HIMU is a rare mantle component that
416 is restricted two OIB locations; St. Helena and Cook-Austal island chain, and thus is unlikely
417 to be a common mixing component in MORB [*Stracke et al*., 2005].

418 Unlike Sr-Nd-Pb isotope composition, the helium isotope characteristic of the
419 enriched basalts from the northern segments cannot be fully explained by the recycling of
420 oceanic crust because radiogenic ingrowth of ^{4}He would lower the $^{3}He/^{4}He$ ratio of the
421 recycled component during its subduction and transport to the ridge. Although $^{3}He/^{4}He$ ratios
422 higher than those of the mantle source for MORB (> $9.0R_A$) are reported for some lavas
423 known as HIMU, those higher helium isotope characteristics are attributed to the involvement
424 of another less-degassed mantle component (e.g. FOZO/C) in addition to recycled crust in the
425 genesis of basalt [*Parai et al.*, 2009]. The radiogenic Pb isotope signature accompanied by
426 elevated $^{3}He/^{4}He$ is also found in the Southeast Indian Ridge (SEIR) lavas, which is locally
427 associated with the Amsterdam–St. Paul (ASP) hotspot that is an example of "C" component
428 [*Graham et al.*, 2014]. Therefore, the elevated $^{3}He/^{4}He$ of the enriched basalts in the northern
429 CIR segments might be associated to FOZO component rather than HIMU.

430 The high $^{3}He/^{4}He$ of the FOZO-like signature in enriched MORB samples from the
431 northern CIR segments is consistent with the model described by *Graham et al.*, [2014] in
432 which they suggested that there is auxiliary upwelling away from plumes, along and near
433 ridges, which can be detected at typical distances of 800-1200 km, in Southeast Indian Ridge
434 and southern East Pacific Rise. The northern CIR segments in this study can be another
435 example of this scale of auxiliary upwelling, given that the distance from the current Reunion

hotspot is quite close to 1000 km. *Malamud and Turcotte* [1999] showed that the large and intermediate size plumes follow a power-law distribution and inferred the existence of many smaller plumes to explain the missing mantle heat flux. Those small plumes may not have the thermochemical buoyancy to generate volcanoes or elevated ridge depth anomalies, and so their upwelling material becomes part of the upper mantle that can ultimately be melted beneath spreading ridges.

6. Conclusions

Trace element and isotope data for MORB from the northern CIR (between 8°S and 17°S) suggest the presence of at least three distinct mantle sources: (1) depleted mantle; (2) an enriched mantle component mainly observed in the southern segments; and (3) a second enriched mantle component in the northern segments. The enrichment signature in the southern segments shows geochemical affinities with the Rèunion plume, located ~1100 km to the west of the ridge. However, the mantle enrichment observed in the southern segments, located north of the MCFZ, appears to be influenced by a fossil Rèunion mantle component, inherited from migration of the CIR over hotspot-modified mantle. In contrast, lavas from the northern segments are compositionally distinct from those of the Rèunion plume, but show isotopic compositions similar to FOZO components. The “FOZO-like” enrichment in the northern segments is consistent with the redefined concept of FOZO as being a ubiquitous component of MORB and OIB sources. The high $^{3}He/^{4}He$ of the FOZO-like signature in enriched MORB samples from the northern CIR segments implies that upper mantle heterogeneity beneath the northern section of the CIR originates from auxiliary upwelling, at ~1000 km distance, of a small plume of deeper mantle that may be dynamically associated with the currently active Rèuinon mantle plume.

Acknowledgments

This research was financially supported by funds from the Ministry of Oceans and Fisheries of Korea (PM59351 and PM58343). We thank scientists and crews of the R/V Onnuri for their support for the sampling and collecting data during the Indian Ridge cruises, Dr. Matthew Cooper of NOC for Sr, Nd, and Pb isotope analyses, and Dr. Marta Zurakowski for He isotope analyses. We are grateful to Jörg Geldmacher, David Graham, William White and a anonymous reviewer for their constructive reviews and Janne Blichert-Toft for editorial handling. We also thank other reviewers of earlier version of manuscript. The geochemical data for this paper are included as two tables in an SI file. Any additional data may be obtained from JK (email: jukim@kiost.ac).

473 References

474 Albarede, F., B. Luais, G. Fitton, M. Semet, E. Kaminski, B. G.J. Upton, P. Bachelery, and J.
475 -L. Cheminee (1997), The geochemical regimes of Piton de la Fournaise Volcano
476 (Rèunion) during the last 530,000 years, *J. Petrol.*, *38*, 171-201, doi:
477 10.1093/petroj/38.2.171.

478 Amante, C., and B. W. Eakins (2009), ETOPO1 1 Arc-Minute Global Relief Model:
479 Procedures, Data Sources and Analysis, NOAA Technical Memorandum NESDIS
480 NGDC-24. National Geophysical Data Center, NOAA, doi:10.7289/V5C8276M.

481 Bosch, D., J. Blichert-Toft, F. Moynier, B. K. Nelson, P. Telouk, P. Gillot, and F. Albarede
482 (2008), Pb, Hf and Nd isotope compositions of the two Rèunion volcanoes (Indian
483 Ocean): A tale of two small-scale mantle "blobs"?, *Earth Planet. Sci. Lett.*, *265*, 748-
484 768, doi:10.1016/j.epsl.2007.11.018.

485 Burnard, P. G., F. M. Stuart, G. Turner, and N. Oskarsson (1994), Air contamination of
486 basaltic magmas – implications for high $^{3}He/^{4}He$ mantle Ar isotopic composition, *J.*
487 *Geophys. Res.*, *99*, 17709-17715, doi:10.1029/94jb01191

488 Chatterjee, S., A. Goswami, and C. R. Scotese (2013), The longest vayage: Tectonic,
489 magmatic, and paleoclimatic evolution of the Indian plate during its northward flight
490 from Gondwana to Asia, *Gondwana Res.*, *23*, 238-267, doi:10.1016/j.gr.2012.07.001.

491 Chauvel, C., W. McDonough, G. Guille, R. Maury, and R. Duncan (1997), Contrasting old
492 and young volcanism in Rurutu Island, Austral chain, *Chem. Geol.*, *139*, 125-143,
493 doi:10.1016/s0009-2541(97)00029-6.

494 DeMets, C., R. G. Gordon, and D. F. Argus (2010), Geologically current plate motions,
495 *Geophys. J. Int.*, *181*, 1-80, doi:10.1111/j.1365-246x.2009.04491.x.

Donnelly, K. E., S. L. Goldstein, C. H. Langmuir, and M. Spiegelman (2004), Origin of enriched ocean ridge basalts and implications for mantle dynamics, *Earth Planet. Sci. Lett.*, *226*, 347-366, doi:10.1016/j.epsl.2004.07.019.

Drolia, R. K., and C. DeMets, C. (2005), Deformation in the diffuse India-Capricorn-Somalia triple junction from a multibeam and magnetic survey of the northern Central Indian Ridge, 3°S -10°S, *Geochem. Geophys. Geosyst.*, *6*, Q09009, doi:10.1029/2005gc000950.

Duncan, R. A. (1990), The volcanic record of the Rèunion hotspot, in: *Proceedings of Ocean Drilling Program Scientific Results*, vol. 115, edited by R. A. Duncan et al., pp. 3-10, College Station, TX, doi:10.2973/odp.proc.sr.115.206.1990.

Dupre, B., and C. J. Allegre (1983), Pb-Sr isotope variations in Indian Ocean basalt and mixing phenomena, *Nature*, *303*, 142-146, doi:10.1016/s0012-821x(01)00379-x.

Dyment, J., Y. Gallet, and the Magofond 2 Scientific Party (1999), The Magofond2 cruise: A surface and deep tow survey on the past and present Central Indian Ridge, *InterRidge News*, *8*, 25-31.

Escrig, S., F. Capmas, B. Dupre, and C. J. Allegre (2004), Osmium isotopic constraints on the nature of the DUPAL anomaly from Indian mid-coean-ridge basalts, *Nature*, *431*, 59-63, doi:10.1038/nature02904.

Fukao, Y. and M. Obayashi (2013), Subducted slabs stagnant above, penetrating through, and trapped below the 660 km discontinuity, *J. Geophys. Res.*, *118*, 5920-5938, doi:10.1002/2013jb010466.

Fukao, Y., S. Widiyantoro, and M. Obayashi (2001), Stagnant slabs in the upper and lower mantle transition region, *Rev. Geophys.*, *39*, 291–323. doi:10.1029/1999rg000068.

Furi, E., D. R. Hilton, B. J. Murton, C. Hemond, J. Dyment, and M. D. Day (2011), Helium isotope variations between Rèunion Island and the Central Indian Ridge (17°-21°S):

New evidence for ridge-hot spot interaction, *J. Geophys. Res.*, *116*, B02207, doi:10.1029/2010jb007609.

Gast, P. W. (1968), Trace element fractionation and the origin of tholeiitic and alkaline magma types, *Geochim. Cosmochim. Acta*, *32*, 1057-1086, doi:10.1016/0016-7037(68)90108-7.

Graham, D. W., J. Lupton, F. Albarede, and M. Condomines (1990), Extreme temporal homogeneity of helium isotopes at Piton de la Fournaise, Rèunion Island, *Nature*, *347*, 545-548, doi:10.1038/347545a0.

Graham, D. W. (2002), Noble gas isotope geochemistry of mid ocean ridge and ocean island basalts: characterization of mantle source reservoirs, *Rev. Mineral. Geochem.*, *47*, 247-317, doi:10.2138/rmg.2002.47.8.

Graham, D. W., B. B. Hanan, C. Hemond, J. Blichert-Toft, and F. Albarede (2014), Helium isotopic textures in Earth's upper mantle, *Geochem. Geophys. Geosyst.*, *15*, 2048-2074, doi:10.1002/2014gc005264.

Grand, S. P., R. van der Hilst, and S. Widiyantoro (1997), Global seismic tomography: A snapshot of convection in the Earth, GSA Today, 7, 1–7.

Greenough, J. D., and B. J. Fryer (1990), Distribution of gold, palladium, platinum, rhodium, and iridium in leg 115 hotspot basalts: Implications for magmatic processes, in: *Proceedings of the Ocean Drilling Program, Scientific Results*, vol. 115, edited by R. A. Duncan et al., pp. 71-84, College Station, TX, doi:10.2973/odp.proc.sr.115.129.1990.

Hanan, B. B., and D. W. Graham (1996), Lead and helium isotope evidence from oceanic basalts for a common deep source of mantle plumes, *science*, *272*, 991-995, doi:10.1126/science.272.5264.991.

543 Hart, S. R. (1971), K, Rb, Cs, Sr and Ba Contents and Sr Isotope Ratios of Ocean Floor
544 Basalts, *Philosophical Transactions of the Royal Society of London. Series A,*
545 *Mathematical and Physical Sciences*, *268*, 573-587, doi:10.1098/rsta.1971.0013.
546 Hart, S. R. (1984), A large scale isotope anomaly in the Southern Hemisphere mantle, *Nature*,
547 *309*, 753-757, doi:10.1038/309753a0.
548 Hart, S. R., E. H. Hauri, L. A. Oschmann, and J. A. Whitehead (1992), Mantle plumes and
549 entrainment: isotopic evidence, *Science*, *256*, 514-520,
550 doi:10.1126/science.256.5056.517.
551 Hauri, E. H., J. A. Whitehead, and S. R. Hart (1994), Fluid dynamic and geochemical aspects
552 of entrainment in mantle plumes, *J. Geophys. Res.*, *99*, 24,275–24,300,
553 doi:10.1029/94JB01257.
554 Hofmann, A. W. (2007), Sampling Mantle Heterogeneity through Oceanic Basalts: Isotopes
555 and Trace Elements, in: *The Mantle and Core*, Treatise on Geochemistry, vol. 2, edited
556 by R.W. Carlson, pp. 1–44, Elsevier, doi: 10.1016/b0-08-043751-6/02123-x.
557 Kawabata, H., T. Hanyu, Q. Chang, J. Kimura, A. R. L. Nichols, and Y. Tatsumi (2011), The
558 petrology and geochemistry of St. Helena alkali basalts: Evaluation of the oceanic crust-
559 recycling model for HIMU OIB, *J. Petrol.*, *52*, 791-838, doi:10.1093/petrology/egr003.
560 Klein, E. M., and C. H. Langmuir (1987), Global correlations of ocean ridge basalt chemistry
561 with axial depth and crustal thickness, *J. Geophys. Res.*, *92*, 8089-8115,
562 doi:10.1029/jb092ib08p08089.
563 Li, M., A. K. McNamara, and E. J. Garnero (2014), Chemical complexity of hotspots caused
564 by cycling oceanic crust through mantle reservoirs, *Nature Geosci.*, *7*, 366-370,
565 doi:10.1038/ngeo02120.

566 Mahoney, J. J., J. H. Natland, W. M. White, R. Poreda, S. H. Bloomer, and A. N. Baxter
567 (1989), Isotopic and geochemical provinces of the western Indian Ocean spreading
568 centers, *J. Geophys. Res.*, *94*, 4033-4052, doi:10.1029/jb094ib04p04033.
569 Malamud, B. D., and D. L. Turcotte (1999), How many plumes are there?, *Earth. Planet. Sci.*
570 *Lett.*, *174*, 113-124, doi:10.1016/s0012-821x(99)00257-5.
571 Matsuda, J., T. Matsumoto, H. Sumino, K. Nagao, J. Yamamoto, Y. Miura, I. Kaneoka, N.
572 Takahata, and Y. Sano (2002), The $^{3}He/^{4}He$ ratio of the new internal He Standard of
573 Japan (HESJ), *Geochem. J.*, *36*, 191-195, doi:10.2343/geochemj.36.191.
574 Murton, B. J., A. G. Tindle, A. Milton, and D. Sauter (2005), Heterogeneity in southern
575 Central Indian Ridge MORB: Implications for ridge-hot spot interation, *Geochem.*
576 *Geophys. Geosyst.*, *6*, Q03E20, doi:10.1029/2004gc000798.
577 Nauret, F., W. Abouchami, S. J. G. Caler, A. W. Hofmann, C. Hemond, C. Chauvel, and J.
578 Dyment (2006), Correlated trace element-Pb isotope enrichments in Indian MORB
579 along 18-20°S, Central Indian Ridge, *Earth Planet. Sci. Lett.*, *245*, 137-152,
580 doi:10.1016/j.epsl.2006.03.015.
581 O'Neill, C., D. Müller, and B. Steinberger (2003), Geodynamic implications of moving
582 Indian Ocean hotspots, *Earth Planet. Sci. Lett.*, *215*, 151-168, doi:10.1016/S0012-
583 821X(03)00368-6.
584 Parai, R., S. Mukhopadhyay, and J. C. Lassiter (2009), New constraints on the HIMU mantle
585 from neon and helium isotopic compositions of basalts from the Cook–Austral Islands,
586 *Earth Planet. Sci. Lett.*, *227*, 253-261, doi:10.1016/j.epsl.2008.10.014.
587 Parson, L. M., P. Patriat, R. C. Searle, and A. R. Briais (1993), Segmentation of the Central
588 Indian Ridge between 12°12′S and the Indian Ocean Triple Junction, *Mar. Geophy. Res.*,
589 *15*, 265–282, doi:10.1007/bf01982385.

590 Schilling, J. -G. (1973), Iceland mantle plume: Geochemical study of Reykjanes Ridge,
591 *Nature*, *242*, 565–571, doi:10.1038/242565a0.
592 Schilling, J. -G. (1985), Upper mantle heterogeneities and dynamics, *Nature*, *314*, 62–67,
593 doi:10.1038/314062a0.
594 Schilling, J. G., and J. W. Winchester (1967), Rare-earth fractionation and magmatic
595 processes, in: *Mantles of Earth and Terrestrial Planets*, edited by S. K. Runcorn, pp.
596 267-283, Intersicence Publishers, London
597 Schilling, J. G., and J. W. Winchester (1969), Rare earth contribution to the origin of
598 Hawaiian lavas, *Contrib. Mineral. Petrol.*, *23*, 27-37, doi:10.1007/bf00371330.
599 Stracke, A., A. W. Hofmann, and S. R. Hart (2005), FOZO, HIMU, and the rest of the mantle
600 zoo, *Geochem. Geophys. Geosyst.*, *6*, Q05007, doi:10.1029/2004gc000824.
601 Stuart, F. M., R. M. Ellam, P. J. Harrop, J. G. Fitton, and B. R. Bell (2000), Constraints on
602 mantle plumes from the helium isotopic composition of basalts from the British Tertiary
603 Igneous Province, *Earth Planet. Sci. Lett.*, *177*, 273-285, doi:10.1016/s0012-
604 821x(00)00050-9.
605 Stuart, F. M., S. Lass-Evans, J. F. Fitton, and R. M. Ellam (2003), High $^{3}He/^{4}He$ ratios in
606 picritic basalts from Baffin Island and the role of a mixed reservoir in mantle plumes,
607 *Nature*, *424*, 57-59, doi:10.1038/nature01711.
608 Sun, S.S., and W. F. McDonough (1989), Chemical and isotopic systematics of oceanic
609 basalt: implications for mantle composition and processes, in: *Magmatism in the*
610 *Oceanic Basins*, Geol. Soc. Spec. Publi., vol. 42, edited by A.D. Saunders, and M.J.
611 Norry, pp. 313-345, The Geological Society, doi:10.1144/gsl.sp.1989.042.01.19.
612 Tanaka, T., S. Togashi, H. Kamioka, H. Amakawa, H. Kagami, T. Hamamoto, M. Yuhara, Y.
613 Orihashi, S. Yoneda, H. Shimizu, T. Kunimaru, K. Takahashi, T. Yanagi, T. Nakano, H.
614 Fujimaki, R. Shinjo, Y. Asahara, M. Tanimizu, and C. Dragusanu (2000), JNdi-1: a

615 neodymium isotopic reference in consistency with LaJolla neodymium, *Chem. Geol.*,
616 *168*, 279-281, 10.1016/s0009-2541(00)00198-4.
617 Taylor, R. N., O. Ishizuka, A. Michalik, J. A. Milton, and I. W. Croudace (2015), Evaluating
618 the precision of Pb isotope measurement by mass spectrometry, *J. Anal. At. Spectrom.*,
619 *30*, 198-213, doi:10.1039/c4ja00279b.
620 Torsvik, T. H., H. Amundsen, E. H. Hartz, F. Corfu, N. Kusznir, C. Gaina, P. V. Doubrovine,
621 B. Steinberger, L. D. Ashwal, and B. Jamtveit (2013), A Precambrian microcontinent in
622 the Indian Ocean. *Nat. Geosci., 6*, 223-227, doi:http://dx.doi.org/10.1038/ngeo1736.
623 Ulrich, M., C. Hémond, P. Nonnotte, and K. P. Jochum (2012), OIB/seamount recycling as a
624 possible process for E-MORB genesis, *Geochem. Geophys. Geosyst., 13*, Q0AC19,
625 doi:10.1029/2012gc004078.
626 Vlastelic, I., K. Koga, C. Chauvel, G. Jacques, and P. Telouk (2009), Survival of lithium
627 isotopic heterogeneities in the mantle supported by HIMU-lavas form Rurutu Island,
628 Austral Chain, *Earth Planet. Sci. Lett., 286*, 456-466, doi:10.1016/j.epsl.2009.07.013.
629 Waters, C. L. , K. W. W. Sims, M. R. Perfit, J. Blichert-Toft, and J. Blusztajn (2011),
630 Perspective on the genesis of E-MORB from chemical and isotopic heterogeneity at 9-
631 10 N East Pacific Rise, *J. Petrol., 52*, 565-602, doi: 10.1093/petrology/egq091.
632 White, W. M., M. M. Cheatham, and R. A. Duncan (1990), Isotope geochemistry of Leg 115
633 basalts and inferences on the history of the Réunion mantle plume, in: *Proceedings of*
634 *the Ocean Drilling Program, Scientific Results*, vol. 115, edited by R. A. Duncan et al.,
635 pp. 53-61, College Station, TX, doi:10.2973/odp.proc.sr.115.131.1990.
636 Williams, A. J., W. M. Phillips, F. M. Stuart, and S. J. Day (2005), Using pyroxene
637 microphenocrysts to determine cosmogenic ^{3}He concentrations in old volcanic rocks: an
638 example of landscape development in central Gran Canaria, *Quat. Sci. Rev.*, 24, 211-222,
639 doi:10.1016/j.quascirev.2004.07.004.

Figure Captions

Figure 1. (A) The index map (modified from ETOPO1 data, *Amante and Eakins*, [2009]) shows the geological setting of the CIR region. (B) Calculated tracks of the Rèunion hotspot based on plate model by *O'Neill et al.*, [2003]. Circled numbers represent 10 Myr intervals. Triangles denote dated sites from ODP legs 115 (age from *Torsvik et al.*, [2013]). Note that the Chagos Lacadives Ridge and the Mascarene Plateau are separated by spreading at the CIR section of this study. (C) Bathymetric map of the Central Indian Ridge (CIR) showing sampling locations. The ridge is divided into seven axial segments along the northern part of the ridge bounded by transform faults. Basalt samples were dredged from the spreading axes of the seven segments bounded by transform faults indicated by dashed lines. Abbreviations: CIR, Central Indian Ridge; SWIR, Southwestern Indian Ridge; SEIR, Southeastern Indian Ridge.

Figure 2. Trace element abundance of basaltic glasses from the study area, normalized to primitive-mantle [*Sun and McDonough*, 1989]. Samples show wide compositional variations, from depleted mid-ocean ridge basalts (N-MORBs) to enriched (E)-MORBs. Dashed lines indicate representative data of basalt from Rèunion Island (averaged value, *Albarede et al.*, [1997]), Gasitao Ridge (D08-1, *Nauret et al.*, [2006)) and a depleted CIR MORB (RC14, *Murton et al.*, [2005])..

Figure 3. Nb/Zr vs. $(La/Sm)_N$ and Ba/La vs. $(La/Sm)_N$ for MORB from CIR 8 to 17°S. The enrichment of basalts from northern and southern segments is not distinguished by proxies for mantle fertility such as Nb/Zr and La/Sm. However, Ba/La ratios are enriched in several MORB from the northern segments, which indicates different enrichment sources (or

664 processes) in northern and southern CIR segments. The color scale is the same as that in
665 Figure 2; i.e. red circles for segments 1-4, gray circles for segment 5, and blue circles for
666 segments 6-7.

667

668 Figure 4. (A–C) Scatter plots of $^{87}Sr/^{86}Sr$ vs. $^{143}Nd/^{144}Nd$, $^{206}Pb/^{204}Pb$ vs. $^{208}Pb/^{206}Pb$, and
669 $^{206}Pb/^{204}Pb$ vs. $^{207}Pb/^{204}Pb$, respectively. Fields from the Central Indian Ridge (CIR), the
670 Carlberg Ridge, the Gasitao Ridge, and the Rèunion Island are shown together with Atlantic
671 and Pacific MORB data for comparison [*Bosch et al.*, 2008; *Nauret et al.*, 2006; *Stracke et al.*,
672 2003]. The color scale is the same as that in Figure 2. Note that enriched samples from the
673 northern segments define a liner array, which differs from the array defined by other samples
674 in both $^{207}Pb/^{204}Pb$–$^{206}Pb/^{204}Pb$ and $^{208}Pb/^{204}Pb$–$^{206}Pb/^{204}Pb$ space. Also, some samples from
675 the northern segments show higher radiogenic Pb isotope compositions than those of Rèunion
676 hotspot samples.

677

678 Figure 5. Latitudinal variations along the ridge axis in chemical compositions of Na_2O
679 calculated at MgO = 8 wt.% (Na_8, as follows *Klein and Langmuir* [1987]), Nb/Yb and La/Sm
680 ratios, and Sr–Nd–Pb-He isotopes (filled circles indicate samples analyzed for Sr–Nd–Pb-He
681 isotopes). Elemental ratios and isotopic compositions both show large fluctuations along the
682 spreading segments, which suggest the existence of variations in mantle fertility beneath the
683 northern CIR. The Sr–Nd–Pb isotopic compositions indicate a general trend of increasing
684 mantle fertility from north to south. However, radiogenic Sr–Pb isotopes are also observed in
685 northern segments (i.e., segment 2 and segment 4 plus the north end of segment 3) where
686 $^{3}He/^{4}He$ are systematically higher than depleted MORB mantle values. Small filled circles in
687 (D) and (J) indicates 4 analyzed samples from the segment 7 by *Furi et al.* [2011].

688

689 Figure 6. (A-C) Helium isotope ratios ($^{3}He/^{4}He$), chondrite normalized La/Sm ratios
690 ($(La/Sm)_N$), and lead isotope ratios ($^{206}Pb/^{204}Pb$) of submarine basalt glasses from the CIR
691 axis of this study (filled dots) and those from the ridge section south of MCFZ (open dots,
692 *Furi et al.*, [2011]; *Nauret et al.*, [2006]). Averaged values of MORB and lavas from Rèunion
693 Island are indicated by the horizontal dashed lines. Helium isotope ratios for MORB mantle
694 (8 ± 1 R_A, *Graham*, [2002]) are indicated as gray shaded zone in (A). Location of Marie
695 Celeste Fracture Zone (MCFZ) is marked as vertical dashed line. Note the lavas near the
696 MCFZ show similar geochemical signatures (i.e. MORB-like $^{3}He/^{4}He$ ratios and enriched
697 La/Sm ratios). Rèunion plume signature is highest in lavas along axis around 19°S, which
698 implies plume flow along beneath the Gasitao Ridge as suggested by *Nauret et al.*, [2006].
699 Enriched basalts from the northern segments, characterized by similar $^{3}He/^{4}He$, lower
700 $(La/Sm)_N$, higher $^{206}Pb/^{204}Pb$ compared to enriched lavas from south of the MCFZ, suggests
701 additional enriched component other than Rèunion plume.

702

703 Figure 7. Diagrams of helium isotopes vs. Sr, Pb isotopes and trace element ratios La/Sm and
704 Ba/La. The majority of basalts from the CIR define a common compositional variation (i.e.
705 slight decrease of $^{3}He/^{4}He$ with increase of radiogenic Sr and Pb isotopes and incompatible
706 trace element ratios (La/Sm and Ba/La)). For reference, the gray line depicts the linear
707 regression for basalts from the southern segments 5 to 7. Some basalts from the northern CIR
708 segments characterized by significantly higher $^{3}He/^{4}He$ than other MORB samples from the
709 CIR. The color scale is the same as that in Figure 2.

710

Figure 8. Diagrams of $^{87}Sr/^{86}Sr$ versus $^{206}Pb/^{204}Pb$ (A and C) and $^{143}Nd/^{144}Nd$ versus $^{208}Pb/^{206}Pb$ (B and D). Two enrichment trends for the basalts from the northern and southern segments are evident in these diagrams. The enrichment patterns observed in the southern segments are similar to those of basalts from the southern CIR, and the data can be extended to data for the Gasitao Ridge and the Rèunion hotspot (*Nauret et al.*, [2006], open circles). The enrichment observed in the northern segments extends towards the Young Rurutu field (open triangles), which represents a FOZO component (A). When plotted with data compiled for ocean basalts [*Stracke et al.*, 2005], the northern and southern enrichments appears to be heading for FOZO and EM2 components, respectively (C). A similar trend exists in a plot of $^{143}Nd/^{144}Nd$ versus $^{208}Pb/^{206}Pb$ (B and D). The color scale is the same as that in Figure 2. Local E-MORBs from the Mid-Atlantic Ridge at ~23°N [*Donnelly et al.*, 2004] and at ~15°20′N [*Ulrich et al.*, 2012] also show "FOZO-like" isotopic trends that are similar to those observed in our data (filled circles in C and D). The shaded green field shows the FOZO composition as redefined by *Stracke et al.* [2005].

Figure 9. $^{87}Sr/^{86}Sr$ versus $^{206}Pb/^{204}Pb$ and La/Sm versus $^{206}Pb/^{204}Pb$ variation diagrams of basalts from the CIR indicating possible mixing between depleted MORB and two enriched components. The majority of basalts from the CIR can be explained by mixing between depleted CIR MORB and fossil Rèunion component. Model composition for fossil Rèunion component is determined from data from Rèunion Trail with an age of 33 Ma (ODP 115 Hole 706, *Greenough and Fryer*, [1990]; *White et al.*, [1990]) with slight modification for missing elements (see Table S3 for model compositions used in plots). Another distinct compositional trend observed in basalts from the northern segments requires an additional enrichment sources characterized by higher radiogenic Pb isotope composition such as HIMU (A and B)

735 or FOZO component (C and D). Primary melt composition of the St. Helena basalts
736 (*Kawabata et al.*, [2011]) and basaltic composition of young Rurutu (*Chauvel et al.*, [1997]
737 and *Vlastelic et al.*, [2009]) are used for model composition representing HIMU and FOZO,
738 respectively (see Table S3). Ticks on the mixing lines correspond to increments of 5%
739 (marked up to 30% of enriched component).

Table 1. Sr, Nd, Pb and He isotopic compositions in MORB glasses from the Central Indian Ridge segment between 8° and 17°S

Sample	segment	Latitude (°S)	Longitude (°E)	Depth (m)	Depth (m)	$^{206}Pb/^{204}Pb$	$^{207}Pb/^{204}Pb$	$^{208}Pb/^{204}Pb$	$^{87}Sr/^{86}Sr$	$^{143}Nd/^{144}Nd$	$^{3}He/^{4}He$ (R/R_A)	^{4}He (ccSTP/g $\times10^{-7}$)*
IR10023501	seg.1	7.94	67.99	3696	3676	18.0682±30	15.4757±29	37.8609±89	0.702783±15	0.513148±5	9.0±0.2	1.1
IR092401g	seg.1	8.06	68.10	3700	3784	18.0749±18	15.4773±18	37.8767±55	0.702768±11	0.513128±5	8.6±0.1	9.3
IR110107	seg.1	8.22	68.24	4440	4503	18.5331±20	15.5351±19	38.3745±59	0.702859±15	0.513110±5	8.7±0.1	33.9
IR092301g	seg.2	9.61	66.65	4092	4230	19.1481±34	15.6146±31	39.0245±99	0.702958±11	0.513035±9	10.2±0.1	78.4
IR092201	seg.2	9.76	66.74	3680	3836	18.1901±20	15.5044±19	37.8625±60	0.702925±18	0.513043±5	9.5±0.1	18.9
IR092202	seg.2	9.76	66.74	3680	3836						9.1±0.1	22.6
IR092101g	seg.2	9.89	66.80	4121	4297	19.1452±20	15.6136±18	38.9996±58	0.702897±11	0.513031±11	11.8±0.1	3.3
IR092102g	seg.2	9.89	66.80	4121	4297						11.0±0.1	5.7
IR091803g	seg.3	10.36	66.30	4268	4327	18.5289±61	15.5283±58	38.3874±181	0.702859±14	0.513084±4	8.0±0.1	10.9
IR091701g	seg.3	10.43	66.36	3909	4125	18.1869±51	15.4840±48	37.9913±150	0.702808±13	0.513080±5	8.4±0.1	43.4
IR091601g	seg.3	10.57	66.48	3488	3517						8.4±0.1	13.4
IR091501g	seg.3	10.71	66.58	3230	3400	18.1614±19	15.4807±18	37.9590±57	0.702780±10	0.513074±8	7.9±0.1	39.6
IR091401g	seg.3	10.85	66.67	3386	3338	18.1545±17	15.4852±17	37.9872±52	0.702843±16	0.513079±5	9.8±0.1	12.1
IR091402g	seg.3	10.85	66.67	3386	3338						9.5±0.1	14.5
IR091404g	seg.3	10.85	66.67	3386	3338						10.6±0.1	6.7
IR10032102	seg.4	11.27	66.57	3370	3398	18.1134±50	15.4714±50	38.0817±150	0.702974±10	0.512989±6	9.1±0.2	0.5
IR110116	seg.4	11.28	66.42	3373	3515						10.6±0.1	23.0
IR110117-1	seg.4	11.28	66.49	3417	3321	18.2722±36	15.5240±35	38.1117±108	0.702928±15	0.513107±5	9.2±0.1	13.7
IR110117-2	seg.4	11.28	66.49	3417	3321						9.3±0.1	29.3
IR110122-1	seg.4	11.35	66.48	3229	3172						10.2±0.1	8.1
IR091101g	seg.4	11.43	66.35	3578	3346	18.1908±23	15.4834±22	38.0137±69	0.702874±16	0.513081±6	9.6±0.2	0.54
IR091001g	seg.4	11.53	66.36	3251	3300	18.9283±32	15.5899±30	38.7896±93	0.702898±10	0.513061±11	9.9±0.1	29.9
IR090701g	seg.5	12.25	65.67	4035	4059	18.0867±32	15.4878±31	37.9976±96	0.702818±12	0.513081±7	7.5±0.1	21.1

IR090501g	seg.5	12.39	65.85	3432	3544	18.3121±18	15.5284±17	38.3557±53	0.702871±11	0.513073±5	7.6±0.1	37.5
IR090401g	seg.5	12.46	65.90	3810	3896	18.3230±18	15.5178±17	38.2136±54	-	0.513098±6	8.4±0.1	44.4
IR090301g	seg.5	12.56	66.03	4215	4371	18.3018±31	15.5168±29	38.2542±91	0.702911±11	0.513202±9	7.7±0.1	3.1
IR110214-1	seg.5	12.84	66.32	2872	2782	17.9895±24	15.4666±23	37.8356±72	0.702817±17	0.513088±6	8.1±0.1	10.7
IR10022901	seg.5	13.04	66.56	3298	3410	18.1133±34	15.4816±33	37.9735±101	0.702871±16	0.513155±10	8.6±0.1	14.9
IR10022701	seg.5	13.25	66.69	3593	3929	17.9054±28	15.4568±27	37.7692±83	0.702816±20	0.513206±12	8.2±0.1	14.3
IR10022401	seg.6	14.08	66.08	3135	3213	18.4750±19	15.5234±18	38.4371±56	0.703097±14	0.512976±9	7.8±0.1	21.2
IR10022101	seg.6	14.58	66.27	3252	3209	18.5960±30	15.5704±30	38.7451±85	-	0.512957±6	7.8±0.1	13.6
IR10021901	seg.6	14.84	66.60	4128	4168	18.3497±25	15.5206±25	38.3769±80	0.703026±16	0.513027±7	8.0±0.1	6.6
IR10021501	seg.6	15.15	66.89	2303	2272	18.1161±29	15.4772±27	37.9700±85	0.702865±13	0.513215±8	9.1±0.1	9.8
IR10021101	seg.6	15.42	67.24	3525	3626	18.0383±82	15.4662±79	37.8704±246	0.702825±10	0.513100±8	9.2±0.1	5.2
IR10020802	seg.6	15.83	67.29	3655	3750	18.0810±50	15.4784±50	37.9478±150	0.702953±13	0.513070±12	8.2±0.1	9.6
IR10020401	seg.7	16.57	66.56	3870	3455	18.4885±28	15.5364±26	38.5189±83	0.703187±13	0.513004±7	8.2±0.1	5.2
IR10020301	seg.7	16.71	66.65	3126	3149	18.2720±28	15.5059±27	38.2310±83	0.703009±14	0.513043±6	8.0±0.1	37.7
IR10020201	seg.7	16.85	66.74	3882	3879	18.4027±29	15.5201±27	38.3376±86	0.703057±11	0.513019±7	7.8±0.1	6.8

* Helium concentrations are minima as the *in vacuo* crushing process did not comminute all samples to powder. Uncertainties are determined from reproducibility of standard (±2%)

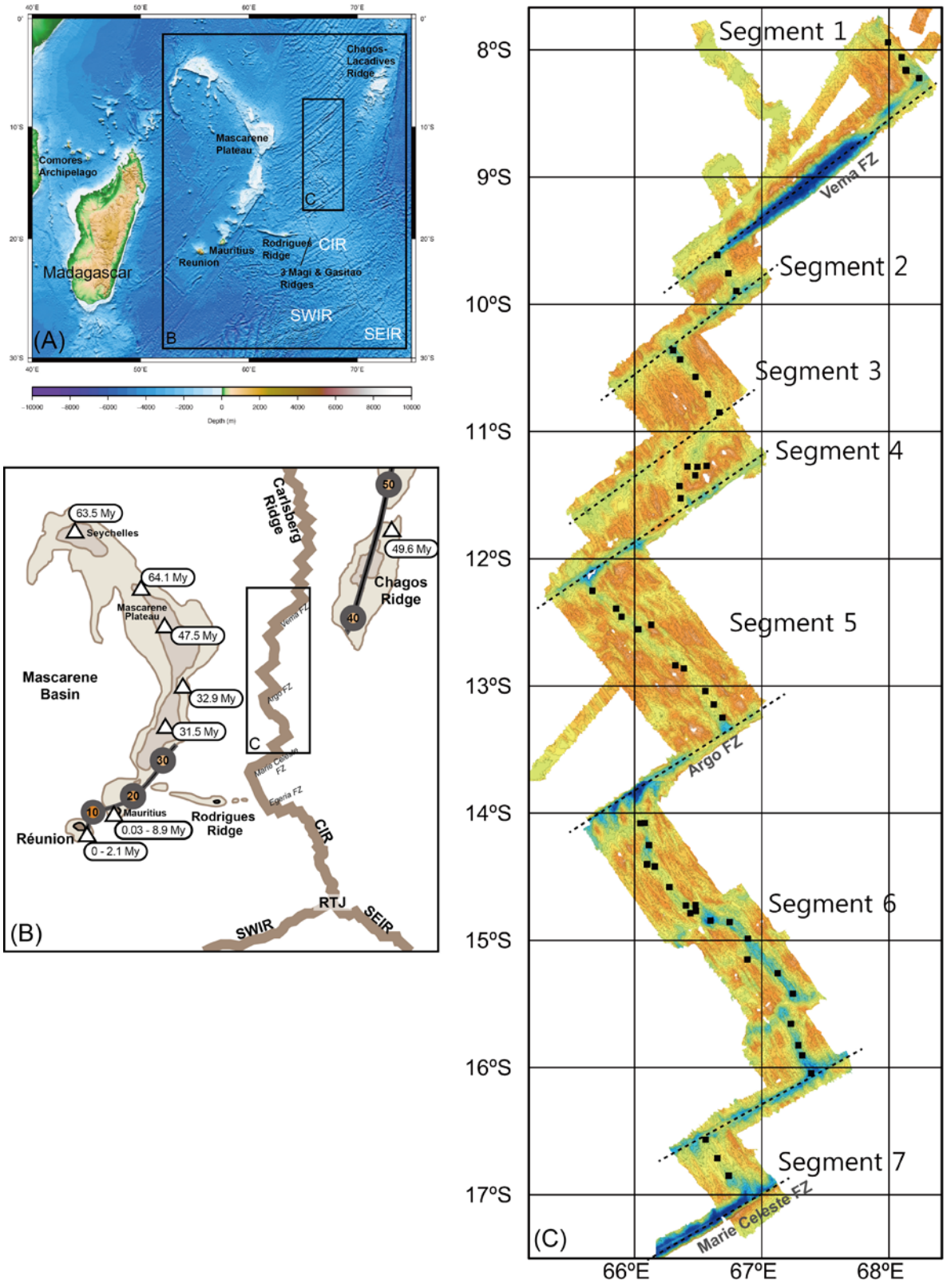
Chagos-
Lacadives
Ridge
Mascarene
Plateau
Comores
Archipelago
Madagascar
Mauritius
Reunion
Rodrigues
Ridge
CIR
3 Magi & Gasitao
Ridges
SWIR
SEIR
(A)
B
C
Depth (m)
63.5 My
Seychelles
64.1 My
Mascarene
Plateau
47.5 My
Mascarene
Basin
32.9 My
31.5 My
Carlsberg
Ridge
50
49.6 My
Chagos
Ridge
40
Vema FZ
Argo FZ
Marie Celeste
FZ
Egeria FZ
30
20
10
Mauritius
0.03 - 8.9 My
Rodrigues
Ridge
Réunion
0 - 2.1 My
CIR
RTJ
SWIR
SEIR
(B)
Segment 1
Segment 2
Segment 3
Segment 4
Segment 5
Segment 6
Segment 7
Vema FZ
Argo FZ
Marie Celeste FZ
8°S
9°S
10°S
11°S
12°S
13°S
14°S
15°S
16°S
17°S
66°E
67°E
68°E
(C)

Figure 1

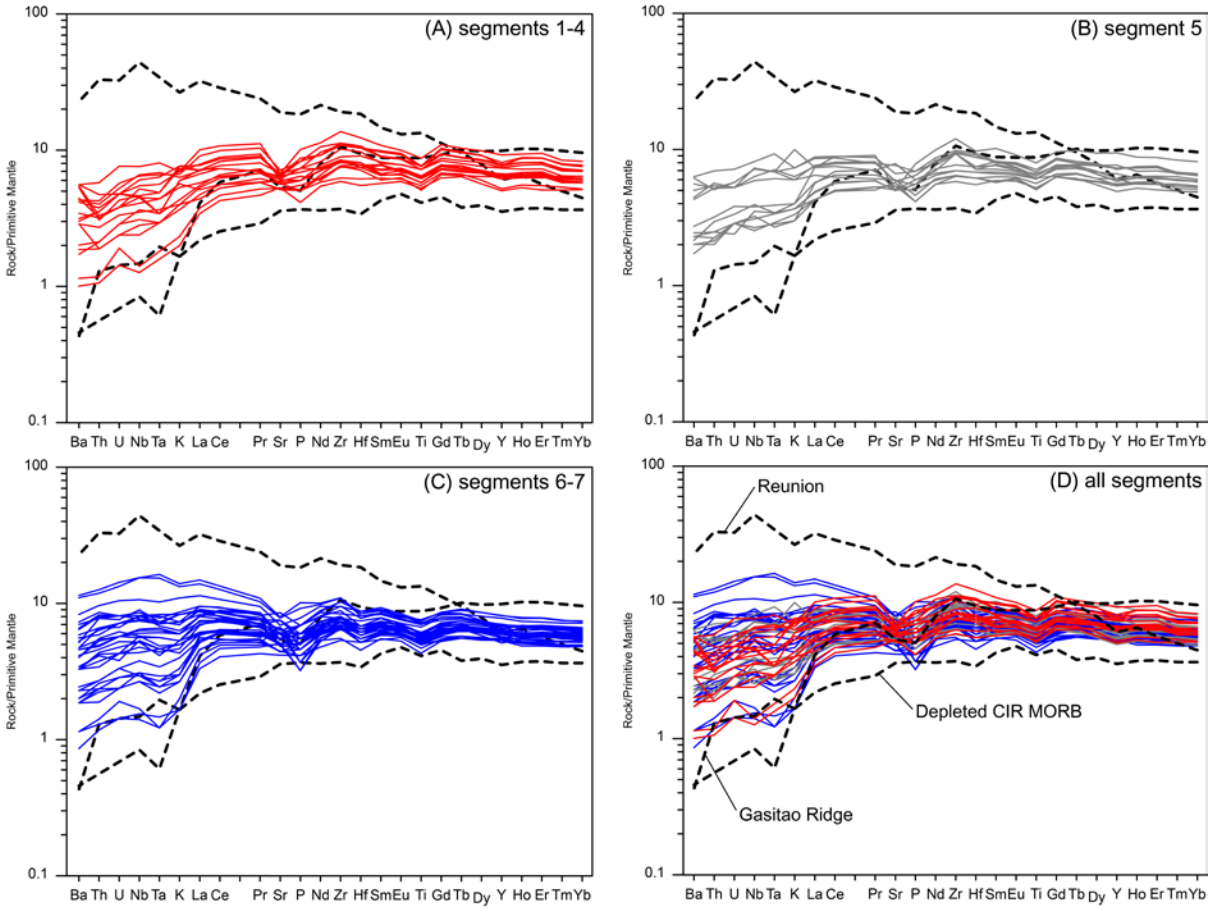
(A) segments 1-4
(B) segment 5
(C) segments 6-7
(D) all segments
Rock/Primitive Mantle
100
10
1
0.1
Ba Th U Nb Ta K La Ce Pr Sr P Nd Zr Hf Sm Eu Ti Gd Tb Dy Y Ho Er Tm Yb
Reunion
Depleted CIR MORB
Gasitao Ridge

Figure 2

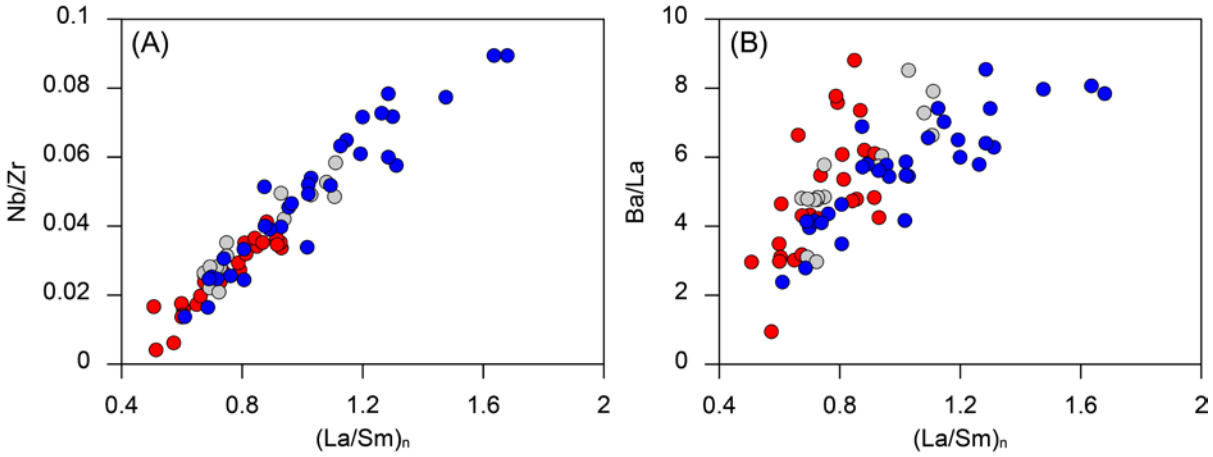
(A)
Nb/Zr
0.1
0.08
0.06
0.04
0.02
0
0.4
0.8
1.2
1.6
2
(La/Sm)n
(B)
Ba/La
10
8
6
4
2
0
0.4
0.8
1.2
1.6
2
(La/Sm)n

Figure 3

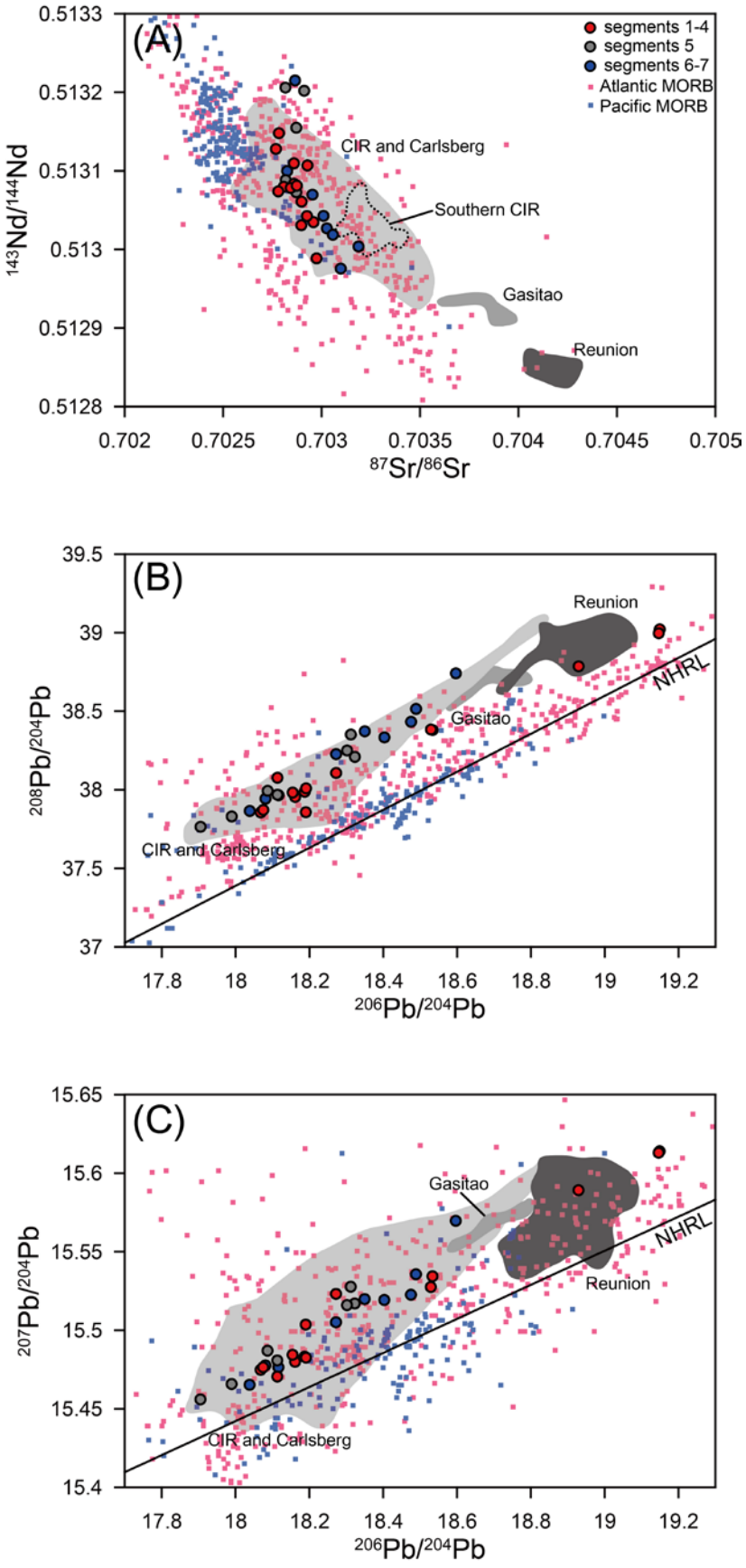
(A)
segments 1-4
segments 5
segments 6-7
Atlantic MORB
Pacific MORB
CIR and Carlsberg
Southern CIR
Gasitao
Reunion
0.5133
0.5132
0.5131
0.513
0.5129
0.5128
143Nd/144Nd
0.702
0.7025
0.703
0.7035
0.704
0.7045
0.705
87Sr/86Sr
(B)
Reunion
NHRL
Gasitao
CIR and Carlsberg
39.5
39
38.5
38
37.5
37
208Pb/204Pb
17.8
18
18.2
18.4
18.6
18.8
19
19.2
206Pb/204Pb
(C)
Gasitao
NHRL
Reunion
CIR and Carlsberg
15.65
15.6
15.55
15.5
15.45
15.4
207Pb/204Pb
17.8
18
18.2
18.4
18.6
18.8
19
19.2
206Pb/204Pb

Figure 4

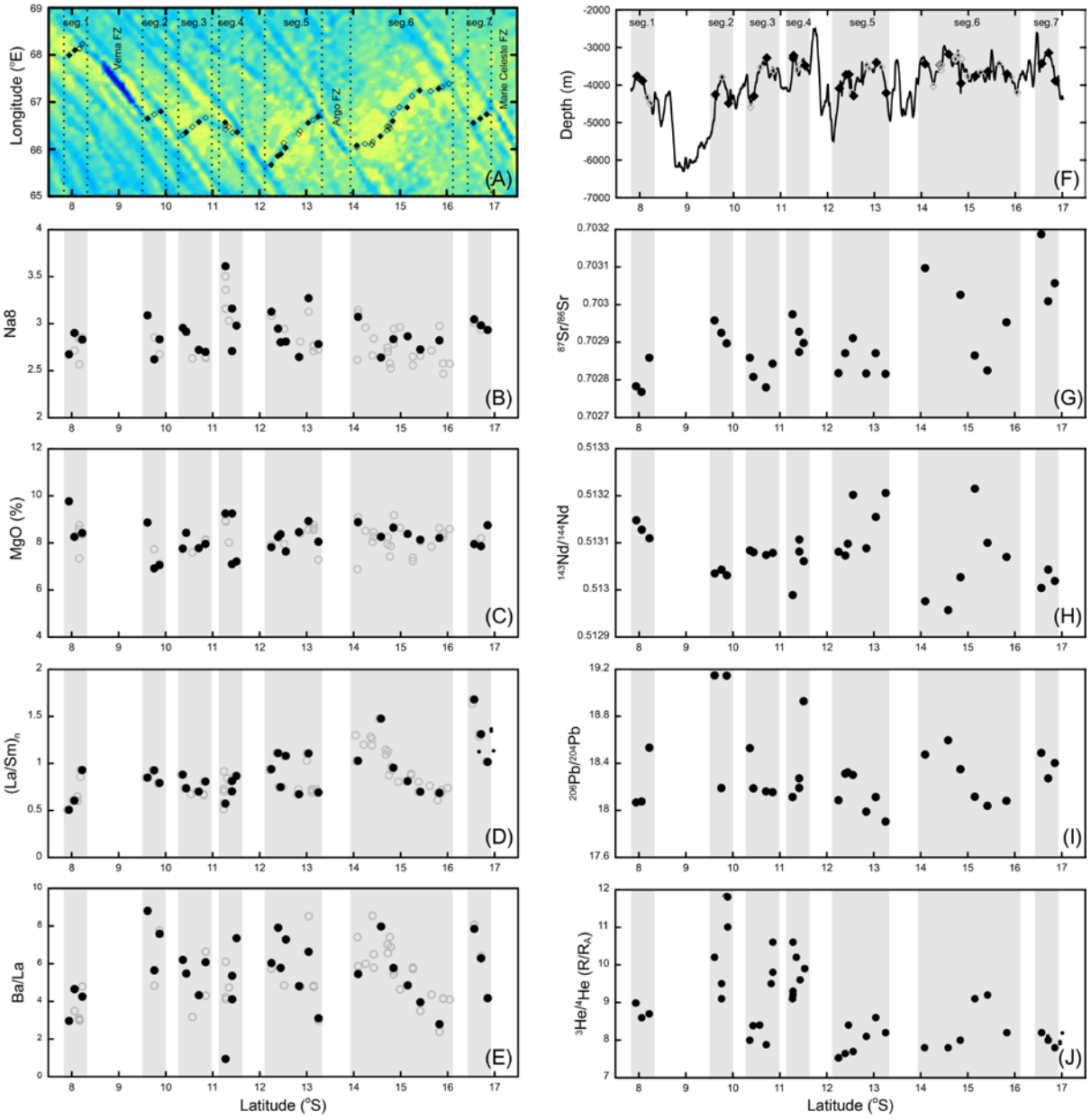
seg.1
seg.2
seg.3
seg.4
seg.5
seg.6
seg.7
Verna FZ
Ago FZ
Marie Celeste FZ
Longitude (°E)
Depth (m)
Na8
$^{87}Sr/^{86}Sr$
MgO (%)
$^{143}Nd/^{144}Nd$
$(La/Sm)_n$
$^{206}Pb/^{204}Pb$
Ba/La
$^{3}He/^{4}He$ (R/R_A)
Latitude (°S)
(A)
(B)
(C)
(D)
(E)
(F)
(G)
(H)
(I)
(J)

Figure 5

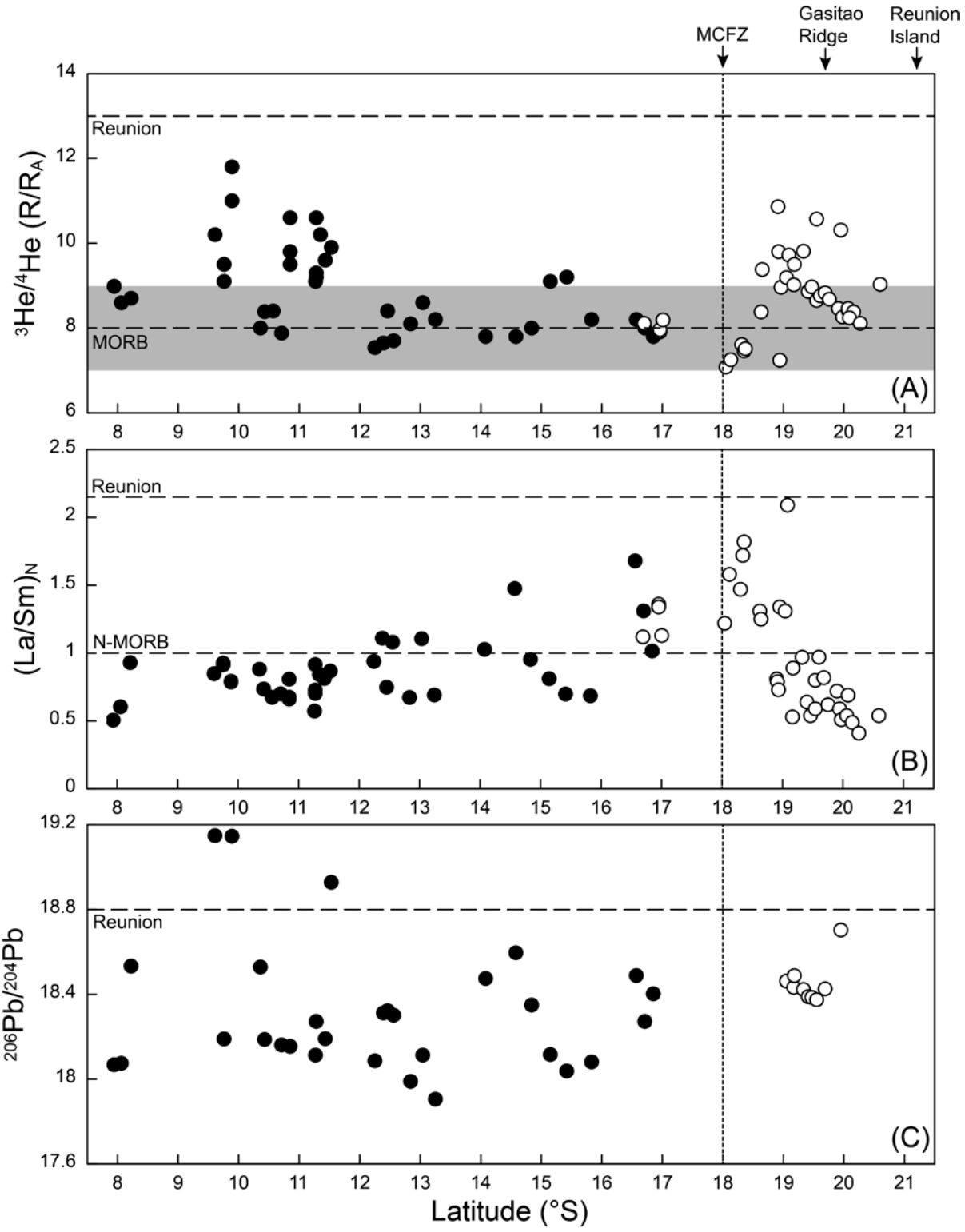
MCFZ
Gasitao Ridge
Reunion Island
Reunion
MORB
(A)
$^{3}He/^{4}He$ (R/R_A)
Reunion
N-MORB
(B)
$(La/Sm)_N$
Reunion
(C)
$^{206}Pb/^{204}Pb$
Latitude (°S)

Figure 6

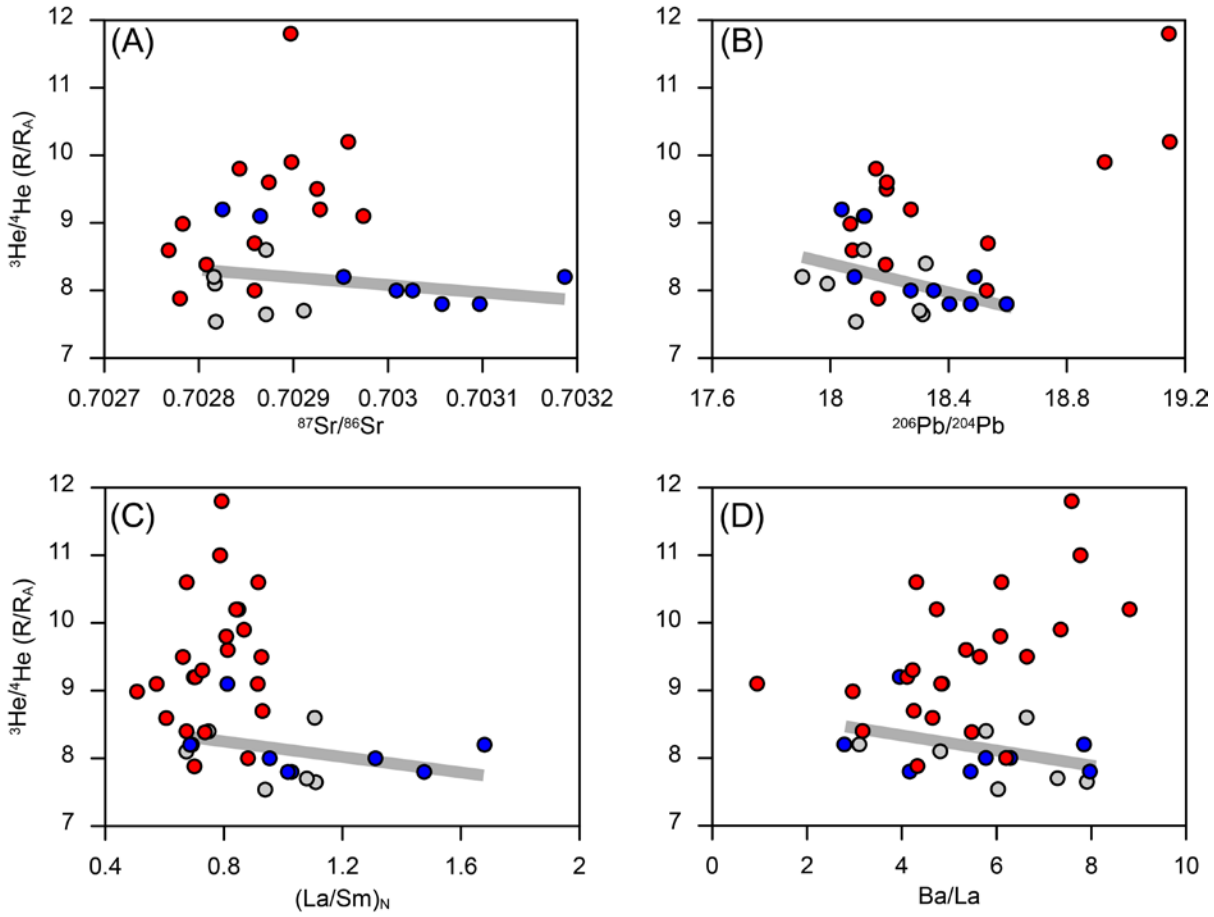
(A)
(B)
(C)
(D)
$^{3}He/^{4}He$ (R/R_A)
$^{87}Sr/^{86}Sr$
$^{206}Pb/^{204}Pb$
$(La/Sm)_N$
Ba/La
12
11
10
9
8
7
0.7027
0.7028
0.7029
0.703
0.7031
0.7032
17.6
18
18.4
18.8
19.2
0.4
0.8
1.2
1.6
2
0
2
4
6
8
10

Figure 7

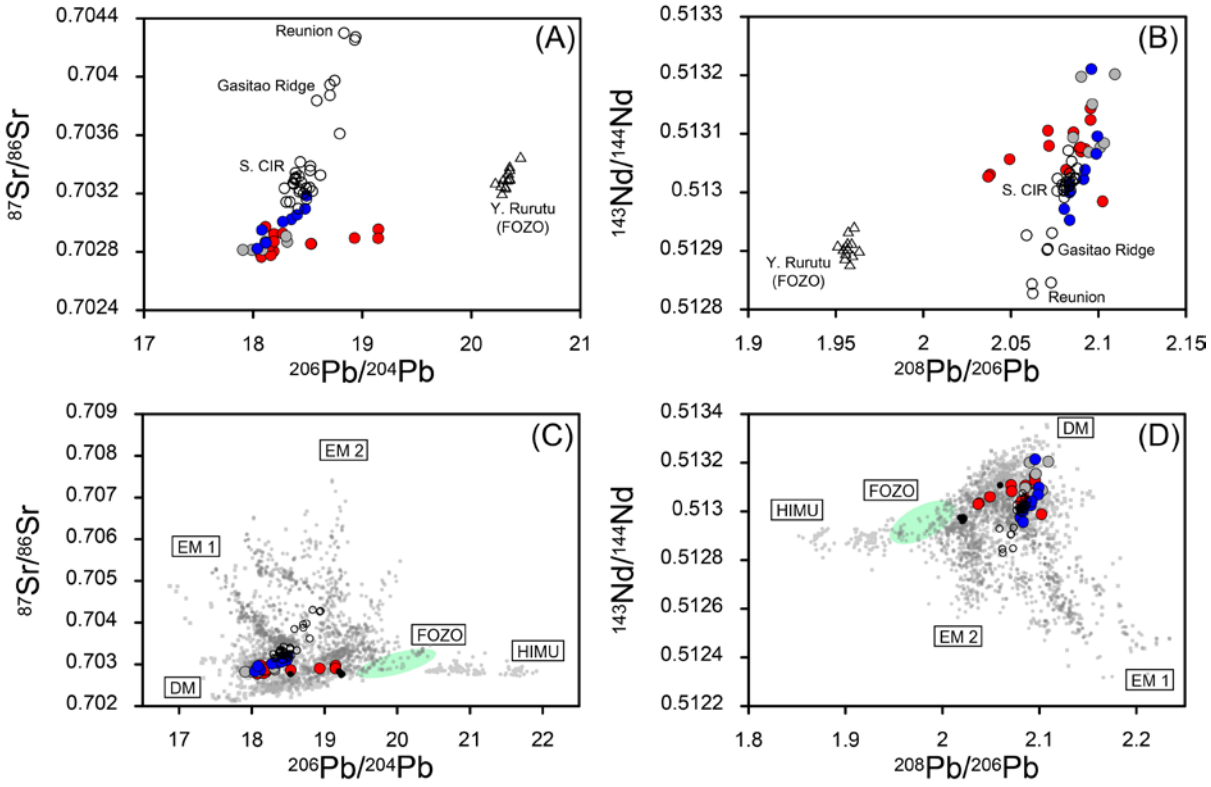
(A)
Reunion
Gasitao Ridge
S. CIR
Y. Rurutu
(FOZO)
87Sr/86Sr
206Pb/204Pb
(B)
S. CIR
Gasitao Ridge
Reunion
Y. Rurutu
(FOZO)
143Nd/144Nd
208Pb/206Pb
(C)
EM 2
EM 1
FOZO
HIMU
DM
87Sr/86Sr
206Pb/204Pb
(D)
DM
FOZO
HIMU
EM 2
EM 1
143Nd/144Nd
208Pb/206Pb

Figure 8

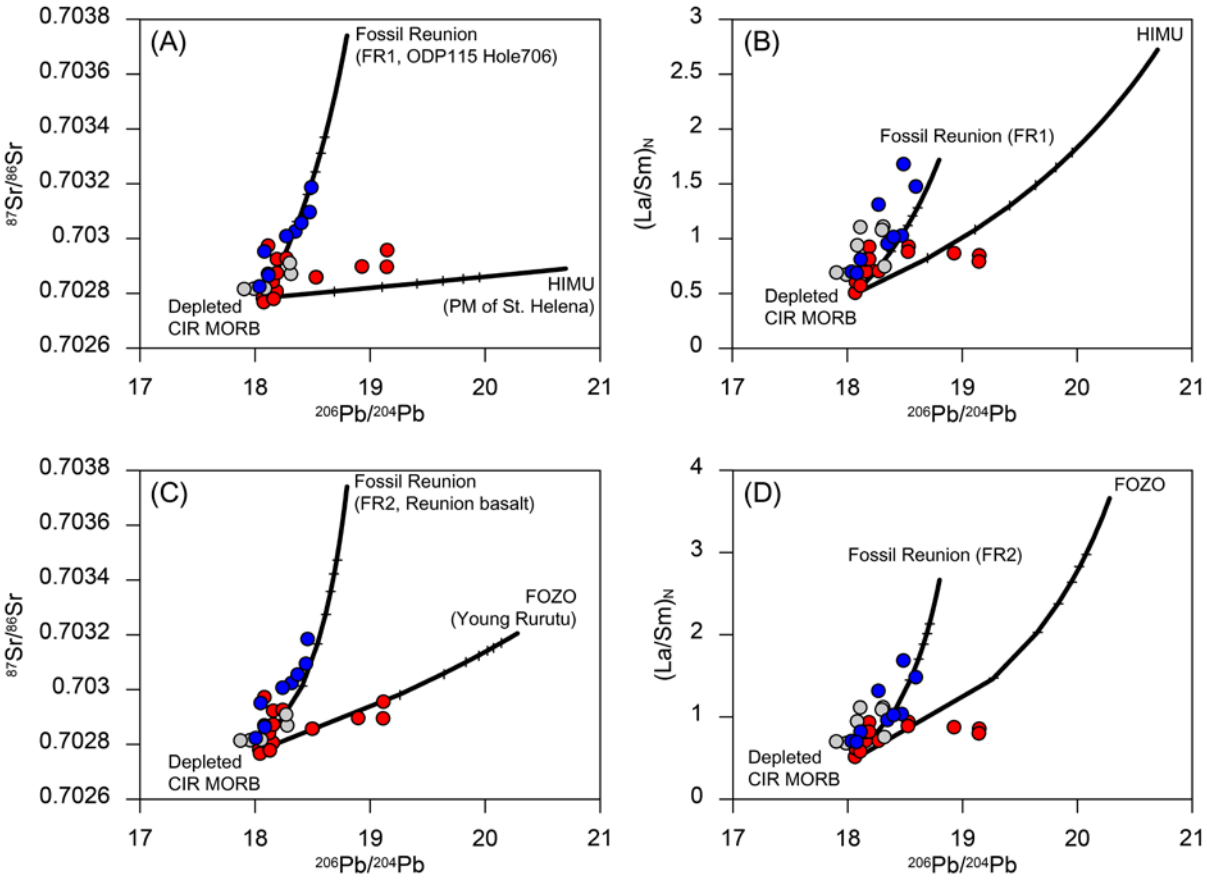
(A)
Fossil Reunion
(FR1, ODP115 Hole706)
HIMU
(PM of St. Helena)
Depleted
CIR MORB
87Sr/86Sr
206Pb/204Pb
(B)
HIMU
Fossil Reunion (FR1)
Depleted
CIR MORB
(La/Sm)N
206Pb/204Pb
(C)
Fossil Reunion
(FR2, Reunion basalt)
FOZO
(Young Rurutu)
Depleted
CIR MORB
87Sr/86Sr
206Pb/204Pb
(D)
FOZO
Fossil Reunion (FR2)
Depleted
CIR MORB
(La/Sm)N
206Pb/204Pb

Figure 9